nature photonics

LETTERS

PUBLISHED ONLINE: 19 AUGUST 2012 | DOI: 10.1038/NPHOTON.2012.190

Enhanced power-conversion efficiency in polymer solar cells using an inverted device structure

Zhicai He, Chengmei Zhong, Shijian Su, Miao Xu, Hongbin Wu* and Yong Cao

Polymer-fullerene bulk heterojunction solar cells (PSCs) are currently attracting a great deal of attention and gaining increasing importance, having already shown great promise as renewable, lightweight and low-cost energy sources[1–4]. Recently, the power-conversion efficiency of state-of-the-art PSCs has exceeded 8% in the scientific literature[5]. However, to find viable applications for this emerging photovoltaic technology, further enhancements in the efficiency towards 10% (the threshold for commercial applications) are urgently required[6]. Here, we demonstrate highly efficient PSCs with a certified efficiency of 9.2% using an inverted structure, which simultaneously offers ohmic contact for photogenerated charge-carrier collection and allows optimum photon harvest in the device. Because of the ease of use and drastic boost in efficiency provided by this device structure, this discovery could find use in fully exploiting the potential of various material systems, and also open up new opportunities to improve PSCs with a view to achieving an efficiency of 10%.

Recently, there have been extensive investigations of polymer solar cells (PSCs) with an inverted device structure, using modified indium tin oxide (ITO) as the cathode (the ITO is modified by n-type metal oxides or metal carbonates[7–13], including titanium oxide, zinc oxide and caesium carbonate, conjugated polyelectrolyte[14–16], self-assembled crosslinked fullerene[17,18] and self-assembled polar molecules[19]). Compared with conventional PSCs, inverted-type devices demonstrate better long-term ambient stability by avoiding the need for the corrosive and hygroscopic hole-transporting poly(3,4-ethylenedioxylenethiophene):poly(styrenesulphonic acid) (PEDOT:PSS) and low-work-function metal cathode, both of which are detrimental to device lifetime[18,20]. Moreover, inverted PSCs can also take advantage of the vertical phase separation and concentration gradient in the active layer[20,21], which is naturally self-encapsulated because air-stable metals are used as the top electrode[9]. The inverted device structure is therefore an ideal configuration for all types of PSCs. Despite these clear benefits, the performances of most inverted PSCs reported to date are inferior to those of regular devices. Indeed, the capability of inverted PSCs to provide independent control of photon harvesting from the Sun's spectrum has not been widely recognized.

In this study, we demonstrate that the efficiency of PSCs can be further enhanced to 9%, an improvement of 10% over the previous record-high efficiency of 8.370% (ref. 5). This is obtained with an inverted device structure, where an alcohol-/water-soluble conjugated polymer, poly [(9,9-bis(3′-(*N*,*N*-dimethylamino)propyl)-2,7-fluorene)-alt-2,7-(9,9–dioctylfluorene)] (PFN)[22] is used as the ITO surface modifier, and a blend of [6,6]-phenyl C_{71}-butyric acid methyl ester ($PC_{71}BM$) and the low-bandgap semiconducting polymer thieno[3,4-*b*]thiophene/benzodithiophene (PTB7)[3] is used as the photoactive layer (see Fig. 1a for device and chemical structure). Unlike previously reported inverted PSCs, which are typically based on n-type metal oxides, our device is solution-processed at room temperature, enabling easy processibility over a large area. Accordingly, the approach is fully amenable to high-throughput roll-to-roll manufacturing techniques, may be used to fabricate vacuum-deposition-free PSCs of large area, and find practical applications in future mass production. Moreover, our discovery overturns a well-accepted belief (the inferior performance of inverted PSCs) and clearly shows that the characteristics of high performance, improved stability and ease of use can be integrated into a single device, as long as the devices are optimized, both optically and electrically, by means of a meticulously designed device structure. We also anticipate that our findings will catalyse the development of new device structures and may move the efficiency of devices towards the goal of 10% for various material systems.

Previously, we reported that PFN can be incorporated into polymer light-emitting devices (PLEDs) to enhance electron injection from high-work-function metals such as aluminium (work function φ of 4.3 eV)[22,23] and has thus been used to realize high-efficiency, air-stable PLEDs[24]. Furthermore, we also found that efficient electron injection can be obtained even in the most noble metals with extremely high work functions, such as gold ($\varphi = 5.2$ eV), by lowering the effective work function (for example lowering φ in gold by 1.0 eV), which has previously been ascribed to the formation of a strong interface dipole[25].

After a thin layer (10 nm) of PFN was applied on top of the ITO, the work function of the ITO was reduced from 4.7 eV to 4.1 eV, as demonstrated by X-ray photoelectron spectroscopy (XPS) measurements (Supplementary Fig. S1). Although the microscopic origin of this reduction in the effective work function of ITO remains uncertain at this point, we speculate that the formation of an interface dipole at the ITO surface as a result of orientation of PFN with a permanent dipole is the major cause for the energy level alignment at the ITO/PFN interface[25,26]. The formation of an interfacial dipole layer can be confirmed by small-angle X-ray diffraction (XRD) (Supplementary Fig. S2). On the other hand, mechanisms[27] such as electron cloud push-back effects, the integer charge-transfer model and the induced density of states model cannot be ruled out at this stage. We also note that a universal model for the energy level alignment of molecules on metal oxides has been developed recently by Greiner and colleagues[28], in which Fermi level-pinning plays a critical role in tuning the energy alignment of a metal oxide. Regardless, as a result of the abrupt shift of vacuum level at the interface (corresponding to a lowering of the effective work function), the modified ITO can form ohmic contact with the photoactive layer and can therefore be used as a cathode for inverted-structure PSCs to facilitate transport and collection of photogenerated charge carriers (Fig. 1b,c).

Figure 2a presents the current density versus voltage (J–V) characteristics of the best PSCs with regular and inverted structures, under 1,000 W m^{-2} air mass 1.5 global (AM 1.5G) illumination.

Institute of Polymer Optoelectronic Materials and Devices, State Key Laboratory of Luminescent Materials and Devices, South China University of Technology, Guangzhou 510640, PR China. *e-mail: hbwu@scut.edu.cn

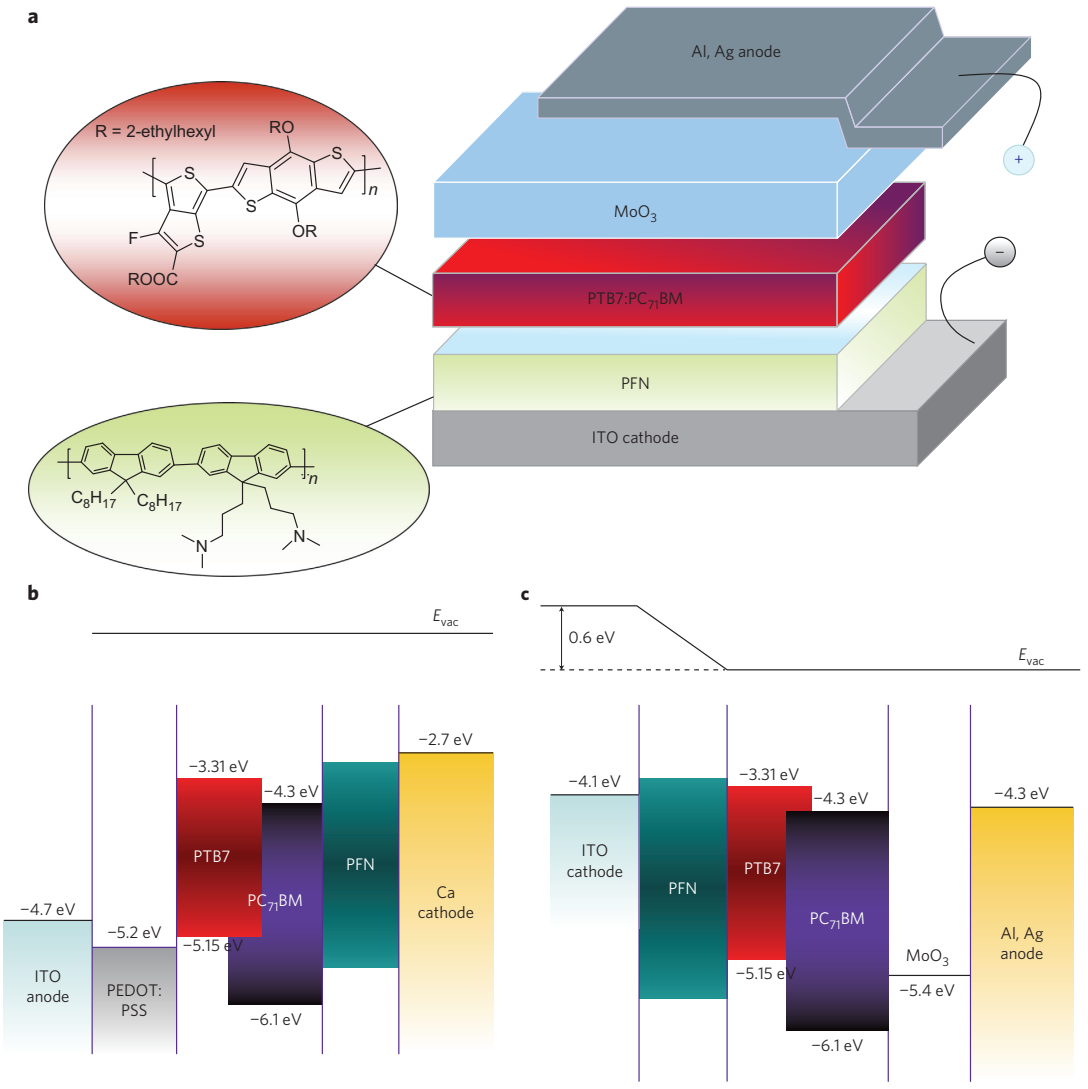

Figure 1 | Device structure and energy levels of the inverted-type PSCs. a, Schematic of the inverted-type PSCs, in which the photoactive layer is sandwiched between a PFN-modified ITO cathode and an Al,Ag-based top anode. Insets: chemical structures of the water-/alcohol-soluble conjugated polymer and electron donor materials used in the study. PFN, poly [(9,9-bis(3′-(*N*,*N*-dimethylamino)propyl)-2,7-fluorene)-alt-2,7-(9,9-ioctylfluorene)]; PTB7: thieno[3,4-*b*]thiophene/benzodithiophene. **b**,**c**, Schematic energy levels of the conventional (**b**) and inverted (**c**) devices under flat band conditions (open-circuit voltage). Note that the formation of a positive interface dipole moment (taking the dipole moment directed outwards to be positive) is presented in **c**.

Device parameters such as J_{SC}, V_{OC}, FF and PCE are deduced from the J–V characteristics (summarized in Table 1). A high average PCE of 8.97±0.10% was achieved in inverted structure devices (with a maximum of 9.15%), while the conventional devices showed an average PCE of 8.06±0.14% (with a highest value of 8.24%, consistent with our previous report[5]). It is clear from Table 1 that the efficiency improvement in the inverted structure devices is mainly due to the higher J_{SC} (17.2 mA cm^{-2} versus 15.4 mA cm^{-2}), because V_{OC} and FF remain nearly the same.

The external quantum efficiency (EQE) curves of the devices are presented in Fig. 2b, with photoresponses with average EQEs of 70% and 63% (in the range 300–700 nm) for the inverted and regular structure devices, respectively. Note that the theoretical J_{SC} values obtained by integrating the product of the EQE data in Fig. 2b and the AM 1.5G solar spectrum are 17.1 mA cm^{-2} and 15.7 mA cm^{-2}, respectively, which are in good agreement with the values obtained from the J–V characteristics (Fig. 2a, Table 1).

After encapsulation, the devices were sent to the National Center of Supervision and Inspection on Solar Photovoltaic Products Quality of China (CPVT) for certification. A certified PCE of 9.214% was obtained (Fig. 2c, Table 1, Supplementary Fig. S3). Notably, another independent testing laboratory NEWPORT Corporation certified a PCE of 8.6±0.3% for a representative device (Supplementary Fig. S3). This result is ~7% lower than that measured in CPVT, which can be attributed to non-ideal cell encapsulation. The results from both external certification laboratories confirmed that the efficiency of our devices is among the highest reported to date for PSCs.

The encapsulated devices were stored in air under ambient conditions and their efficiency measured periodically to assess their long-term stability (Supplementary Fig. S4). The inverted device retained 95% of its initial efficiency (9.00%) after exposure to air for 62 days, whereas the regular devices lost half their initial efficiency after 10 days. This demonstrates that the inverted PSCs can achieve a high efficiency of 9% and also maintain good ambient stability.

The drastically enhanced J_{SC} in the inverted PSCs may originate from reduced bimolecular recombination[29,30] or increased absorption of photons[1], or indeed a combination of both. The increase in optical absorption was confirmed by optical modelling

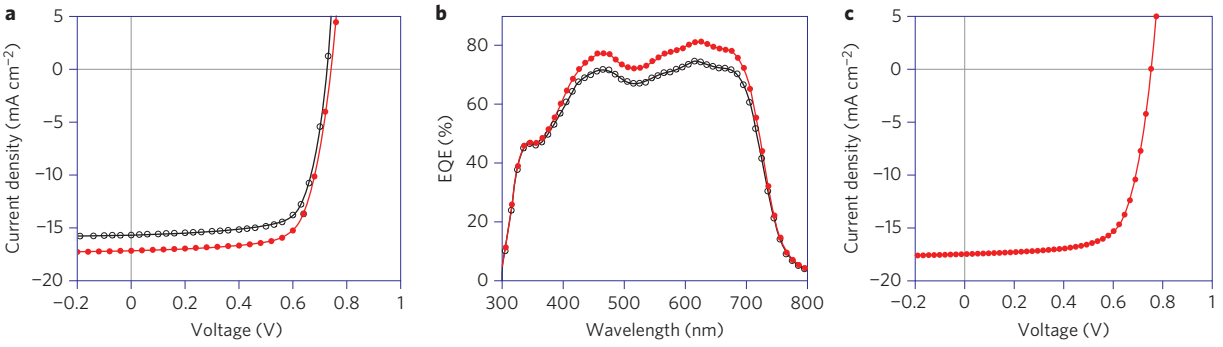

Figure 2 | Device performances of the inverted structure (ITO/PFN interlayer/active layer/MoO_3 (10 nm)/Al) PTB7:$PC_{71}BM$ PSCs and the conventional device (ITO/PEDOT:PSS/active layer/PFN interlayer/Ca/Al). a, Current density versus voltage (*J*–*V*) characteristics under 1,000 W m^{-2} AM 1.5G illumination for conventional (open symbols) and inverted (filled symbols) devices. **b**, EQE/IPCE spectra for conventional (open symbols) and inverted (filled symbols) devices. **c**, CPVT-certified *J*–*V* characteristics of an inverted structure PTB7:$PC_{71}BM$ solar cells, with a PCE of 9.214%.

Table 1 | Best device performance/parameters from PTB7:$PC_{71}BM$ solar cells with conventional and inverted device structures, measured under 1,000 W m^{-2} AM 1.5G illumination.

Device type	PCE (%)	J_{SC} (mA cm^{-2})	FF (%)	V_{OC} (V)
Conventional	8.24	15.4	70.6	0.759
Inverted	9.15	17.2	72.0	0.740
Inverted, tested by CPVT	9.214	17.46	69.99	0.754

calculations (Fig. 3) in which a one-dimensional transfer matrix formalism (TMF) was applied[31] and experimentally measured refractive indices and extinction coefficients were used. Figure 3a depicts the absorbed incident photon flux density in both devices, each with a 100-nm-thick active layer, verifying that the inverted structure can harvest more photons from solar spectra than the regular devices. Furthermore, it can be seen from Fig. 3b that the inverted device always has a higher J_{SC} than the regular devices, regardless of the active layer thickness, demonstrating the advantage of the inverted device structure.

The stronger absorption in the inverted device can also be verified experimentally by reflectance spectra measurements on real devices (Supplementary Fig. S5); the inverted devices show a decreased reflectance over a wide range of spectra (400–800 nm) when compared with the regular device.

The calculated maximum J_{SC} of the inverted device under AM 1.5G illumination (440–800 nm) as a function of interlayer thickness is presented in Supplementary Fig. S6b, and the performances of devices with varied PFN thickness (5, 10 and 20 nm) are shown in Supplementary Fig. S6a and Table S1. Although the theoretical J_{SC} is not sensitive to PFN layer thickness, the overall performance critically depends on this thickness. This is understandable, because an interlayer that is too thick will lead to a high series resistance, while a too-thin layer could not provide an ohmic contact for electron extraction.

Both types of devices exhibit very high FF (70%) and demonstrate a comparable dependence on incident light intensity (Supplementary Fig. S7), implying that any difference in charge-carrier recombination loss in the devices can be neglected. It can therefore be concluded that the 10% increase in J_{SC} is mainly due to enhanced optical absorption as a result of the redistribution of the electric field intensity of the incident photons inside the active layer[31].

To gain further insight into the origin of the enhanced J_{SC} in the device, we determined the experimental photocurrent generation rate (G) in the devices. Given that the saturation photocurrent densities (J_{sat}) for the regular and inverted devices are 16.7 mA cm^{-2} and 18.6 mA cm^{-2}, respectively (Supplementary Fig. S8), the

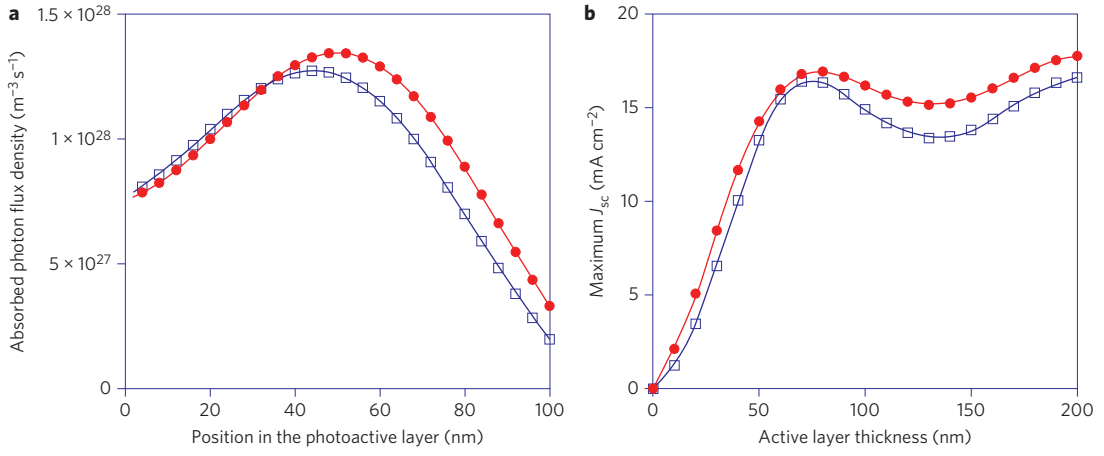

Figure 3 | Comparison of calculated optical absorption profile for conventional and inverted devices. Conventional device: ITO/PEDOT:PSS (40 nm)/PTB7:$PC_{71}BM$ (100 nm)/PFN (5 nm)/Al (100 nm); inverted device: ITO/PFN(10 nm)/PTB7:$PC_{71}BM$ (100 nm)/MoO_3 (10 nm)/Al (100 nm). **a**, Distribution of absorbed AM 1.5G photon flux density inside the active layer. **b**, Variation of maximum J_{SC} with active layer thickness for two types of devices, both under AM 1.5G illumination (440–800 nm). Open squares and filled circles represent conventional and inverted devices, respectively.

maximal obtainable exciton generation rates can be determined as 1.30×10^{28} m^{-3} s^{-1} and 1.45×10^{28} m^{-3} s^{-1}, respectively. In other words, the experimental absorbed incident photon flux density in the active layer in the inverted device is indeed ~10% higher than that of the regular device, which is in good agreement with the observed J_{SC} and the reflectance spectra of the devices shown in Supplementary Fig. S5.

For comparison, we also fabricated inverted devices using ZnO as an electron-selective cathode following a well-established procedure that required high-temperature annealing[11]. The devices based on PFN also show superior performance over the ZnO-based devices (9.15% versus 8.35%, with the ZnO device showing a PCE of 8.34 ± 0.04%, with a maximum of 8.39%; Supplementary Fig. S9 and Table S2), mainly due to a more efficient photon harvest in this device structure (Supplementary Fig. S5).

Our approach can also be used for semitransparent PSCs[7,8,10]. On the basis of the abovementioned inverted PSCs, highly efficient semitransparent PSCs were fabricated, with the highly reflective anode MoO_3 (10 nm)/Al (100 nm) replaced by a transparent layer of MoO_3 (10 nm)/Ag (20 nm). The *J–V* characteristics of the semitransparent PSCs, under front- and rear-side AM 1.5G illumination, are presented in Fig. 4. The PCE values for the device under front-, and rear-side illumination are 6.13% and 4.96%, respectively. We anticipate that our prototype of semitransparent PSCs will find practical applications in building windows, foldable curtains and invisible electronic circuits[10].

In conclusion, we have successfully demonstrated highly efficient PSCs with a certified efficiency of 9.2% using a straightforward inverted structure, in which an alcohol-/water-soluble conjugated polymer is used to tune the work function of ITO. By using experimental photocurrent measurements in combination with optical modelling based on a one-dimensional TMF, we have demonstrated that, as well as offering ohmic contact for photogenerated charge-carrier collection, the inverted structure can provide optimum photon harvest from the sun's spectrum. Because of a remarkably improved J_{SC} of >17 mA cm^{-2}, the inverted PSCs exhibit a superior overall device performance when compared to regular devices, as well as good ambient stability. It is worth noting that, according to our calculation, a further increase of 10% in J_{SC} could be obtained if the optical constants of the interlayer were matched with those of the stacks of other layers. In the quest to optimize device performance of PSCs, both optically and electrically, we anticipate that our findings will catalyse the development of new device structures and may further pushing the efficiency of devices towards the goal of 10% with various material systems.

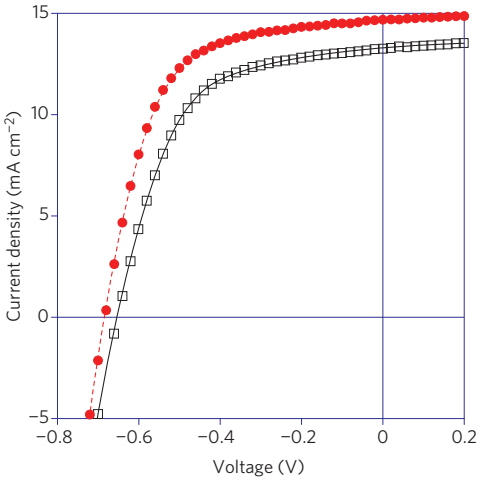

Figure 4 | *J–V* characteristics for semitransparent PSCs under front- and rear-side AM 1.5G (1,000 W m^{-2}) illumination. Open squares and filled circles represent conventional and inverted devices, respectively.

Methods

Fabrication of PSCs. Electron donor material PTB7 and electron acceptor $PC_{71}BM$ were purchased from 1-material Chemscitech and Aldrich, respectively, and used as received. The PEDOT:PSS (Clevios P AI4083) was obtained from H.C. Starck Clevios. The inverted device structure was ITO/PFN/PTB7:$PC_{71}BM$(1:1.5 by weight)/MoO_3/Al or Ag and the regular device structure was ITO/PEDOT:PSS/PTB7:$PC_{71}BM$/PFN/Ca/Al (ref. 5). The PFN interlayer material was dissolved in methanol in the presence of a small amount of acetic acid (2 μl ml^{-1}) and its solution (concentration, 2 mg ml^{-1}) was spin-coated on top of the precleaned ITO substrate, which was treated by oxygen plasma cleaning for 4 min. For regular devices, a 40-nm-thick PEDOT:PSS anode buffer layer was spin-cast on the ITO substrate, then dried in a vacuum oven at 80 °C overnight. The PTB7:$PC_{71}BM$ active blend layer, with a nominal thickness of ~80 nm (with a variation of ~20 nm over the entire film), was prepared by spin-coating a mixed solvent of chlorobenzene/1,8-diiodoctane (97:3% by volume)[3] solution (concentration, 25 mg ml^{-1}) at 1,000 r.p.m. for 2 min. A 10 nm MoO_3 layer and a 100 nm Al or Ag (20 nm for semitransparent device) layer were subsequently evaporated through a shadow mask to define the active area of the devices (~2 × 8 mm^2) and form a top anode.

Characterization and measurements. PCE values were determined from *J–V* curve measurements (using a Keithley 2400 source meter) under a 1 sun, AM 1.5G spectrum from a solar simulator (Oriel model 91192; 1,000 W m^{-2}). Masks were made using laser beam cutting technology and had well-defined areas of 3.14 or 16.0 mm^2; these were attached to define the effective area for accurate measurement. All masked and unmasked tests gave consistent results with relative errors within 5%. Solar simulator illumination intensity was determined using a monocrystal silicon reference cell (Hamamatsu S1133, with KG-5 visible colour filter) calibrated by the National Renewable Energy Laboratory (NREL). Theoretical J_{SC} values obtained by integrating the product of the EQE with the AM 1.5G solar spectrum agreed with the measured value to within 3%. Spectral mismatch factors (*M*) were calculated according to a standard procedure[32], and an *M* value of 1.03 was used to obtain the correct photocurrent and efficiency for the PTB7 devices.

For small-angle XRD analysis, a Bruker D8 advance X-ray diffractometer with CuKα radiation was used (operating conditions: 40 kV and 40 mA). The diffractometer was equipped with a solid-state detector (LynxExe 1D) that facilitated high count rates and short measuring time. XPS studies were performed on a Thermo-VG Scientific ESCALAB 250 photoelectron spectrometer using a monochromated AlKα (1,486.6 eV) X-ray source. All recorded peaks were corrected for electrostatic effects by setting the C–C component of the C_{1s} peak to 284.8 eV. The base pressure in the XPS analysis chamber was $<2 \times 10^{-9}$ mbar. Typical atomic force microscopy (AFM) topography images of the MoO_3 deposited on top of the active layer are shown in Supplementary Fig. S11. The films are generally smooth, with a root-mean-square (r.m.s.) roughness of 0.48 nm, implying that significant scattering at the MoO_3 interface is unlikely to occur.

The one-dimensional spatial distribution of normalized incident light intensity ($|E|^2$) inside the devices was calculated by means of an optical TMF approach[31]. The spatial distribution of the absorbed photon flux density could then be calculated by integrating single-wavelength $|E|^2$ with an AM 1.5G spectrum from 440 nm to 800 nm. Finally, the theoretical maximum J_{sc} for a device under AM 1.5G illumination was determined by spatially integrating the absorbed photon flux density within the active layer, assuming 100% internal quantum efficiency for all wavelengths. The refractive index (*n*) and extinction coefficient (*k*) spectra (440–840 nm) for each layer in the devices were experimentally determined using a Horiba Jobin Yvon AUTO SE ellipsometer, and most data are shown in Supplementary Fig. S12. The reflection spectra of the devices were recorded using an UV–vis–NIR spectrophotometer (Lambda750, PerkinElmer).

Received 25 March 2012; accepted 6 July 2012;
published online 19 August 2012

References

1. Park, S. H. *et al.* Bulk heterojunction solar cells with internal quantum efficiency approaching 100%. *Nature Photon.* **3,** 297–303 (2009).
2. Chen, H-Y. *et al.* Polymer solar cells with enhanced open-circuit voltage and efficiency. *Nature Photon.* **3,** 649–653 (2009).
3. Liang, Y. Y. *et al.* For the bright future-bulk heterojunction polymer solar cells with power conversion efficiency of 7.4%. *Adv. Mater.* **22,** E135–E138 (2010).
4. Seo, J.-H. *et al.* Improved high-efficiency organic solar cells via incorporation of a conjugated polyelectrolyte interlayer. *J. Am. Chem. Soc.* **133,** 8416–8419 (2011).
5. He, Z. C. *et al.* Simultaneous enhancement of open-circuit voltage, short-circuit current density and fill factor in polymer solar cell. *Adv. Mater.* **23,** 4636–4643 (2011).
6. Brabec, C. J. *et al.* Polymer–fullerene bulk-heterojunction solar cells. *Adv. Mater.* **22,** 3839–3856 (2010).

7. Li, G., Chu, C. W., Shrotriya, V., Huang, J. & Yang, Y. Efficient inverted polymer solar cells. *Appl. Phys. Lett.* **88,** 253503 (2006).
8. Waldauf, C. *et al.* Highly efficient inverted organic photovoltaics using solution based titanium oxide as electron selective contact. *Appl. Phys. Lett.* **89,** 233517 (2006).
9. Huang, J., Li, G. & Yang, Y. A semi-transparent plastic solar cell fabricated by a lamination process. *Adv. Mater.* **20,** 415–419 (2008).
10. Ameri, T. *et al.* Fabrication, optical modeling, and color characterization of semitransparent bulk-heterojunction organic solar cells in an inverted structure. *Adv. Funct. Mater.* **20,** 1592–1598 (2010).
11. Yang, T. B. *et al.* Solution-processed zinc oxide thin film as a buffer layer for polymer solar cells with an inverted device structure. *J. Phys. Chem. C* **114,** 6849–6853 (2010).
12. Sun, Y. M., Seo, J. H., Takacs, C. J., Seifter, J. & Heeger, A. J. Inverted polymer solar cells integrated with a low-temperature-annealed sol-gel-derived ZnO film as an electron transport layer. *Adv. Mater.* **23,** 1679–1683 (2011).
13. Small, C. E. *et al.* High-efficiency inverted dithienogermole–thienopyrrolodione-based polymer solar cells. *Nature Photon.* **6,** 115–120 (2012).
14. Na, S-I., Kim, T. S., Oh, S-H., Kim, J-Y., Kim, S-S. & Kim, D-Y. Enhanced performance of inverted polymer solar cells with cathode interfacial tuning via water-soluble polyfluorenes. *Appl. Phys. Lett.* **97,** 223305 (2010).
15. Choi, H. S. *et al.* Combination of titanium oxide and a conjugated polyelectrolyte for high-performance inverted-type organic optoelectronic devices. *Adv. Mater.* **23,** 2759–2763 (2011).
16. Zhu, Y. X., Xu, X. F., Zhang, L. J., Chen, J. W. & Cao, Y. High efficiency inverted polymeric bulk-heterojunction solar cells with hydrophilic conjugated polymers as cathode interlayer on ITO. *Sol. Ener. Mater. Sol. Cells* **97,** 83–88 (2012).
17. Cheng, Y.-J., Hsieh, C.-H., He, Y. J., Hsu, C.-S. & Li, Y. F. Combination of indene–C_{60} bis-adduct and cross-linked fullerene interlayer leading to highly efficient inverted polymer solar cells. *J. Am. Chem. Soc.* **132,** 17381–17383 (2010).
18. Hsieh, C.-H. *et al.* Highly efficient and stable inverted polymer solar cells integrated with a cross-linked fullerene material as an interlayer. *J. Am. Chem. Soc.* **132,** 4887–4893 (2010).
19. Park, J. S. *et al.* Efficient hybrid organic-inorganic light emitting diodes with self-assembled dipole molecule deposited metal oxides. *Appl. Phys. Lett.* **96,** 243306 (2010).
20. Xu, Z. *et al.* Vertical phase separation in poly(3-hexylthiophene): fullerene derivative blends and its advantage for inverted structure solar cells. *Adv. Funct. Mater.* **19,** 1227–1234 (2009).
21. Campoy-Quiles, M. *et al.* Morphology evolution via self-organization and lateral and vertical diffusion in polymer:fullerene solar cell blends. *Nature Mater.* **7,** 158–164 (2008).
22. Huang, F., Wu, H. B., Wang, D. L., Yang, W. & Cao, Y. Novel electroluminescent conjugated polyelectrolytes based on polyfluorene. *Chem. Mater.* **16,** 708–716 (2004).
23. Wu, H. B. *et al.* Efficient electron injection from a bilayer cathode consisting of aluminum and alcohol-/water-soluble conjugated polymers. *Adv. Mater.* **16,** 1826–1830 (2004).
24. Huang, F., Wu, H. B. & Cao, Y. Water/alcohol soluble conjugated polymers as highly efficient electron injection/transporting layer in optoelectronic devices. *Chem. Soc. Rev.* **39,** 2500–2521 (2010).
25. Wu, H. B., Huang, F., Peng, J. B. & Cao, Y. High-efficiency electron injection cathode of Au for polymer light-emitting devices. *Org. Elect.* **6,** 118–128 (2005).
26. Ishii, H., Sugiyama, K., Ito, E. & Seki, K. Energy level alignment and interfacial electronic structures at organic/metal and organic/organic interfaces. *Adv. Mater.* **11,** 605–625 (1999).
27. Braun, S., Salaneck, W. R. & Fahlman, M. Energy-level alignment at organic/metal and organic/organic interfaces. *Adv. Mater.* **21,** 1450–1472 (2009).
28. Greiner, M. T. *et al.* Universal energy-level alignment of molecules on metal oxides. *Nature Mater.* **11,** 76–81 (2012).
29. Blom, P. W. M., Mihailetchi, V. D., Koster, L. J. A. & Markov, D. E. Device physics of polymer:fullerene bulk heterojunction solar cells. *Adv. Mater.* **19,** 1551–1566 (2007).
30. Shuttle, C. G., Hamilton, R., O'Regan, B. C., Nelson, J. & Durrant, J. R. Charge-density-based analysis of the current–voltage response of polythiophene/fullerene photovoltaic devices. *Proc. Natl Acad. Sci. USA* **107,** 16448–16452 (2010).
31. Pettersson, L. A. A., Lucimara, S. R. & Inganas, O. Modeling photocurrent action spectra of photovoltaic devices based on organic thin films. *J. Appl. Phys.* **86,** 487–496 (1999).
32. Shrotriya, V. *et al.* Accurate measurement and characterization of organic solar cells. *Adv. Funct. Mater.* **16,** 2016–2023 (2006).

Acknowledgements

The authors thank Min Yun of the National Center of Supervision and Inspection on Solar Photovoltaic Products Quality for device performance verification, Fangyan Xie of Sun Yat-San University for XPS measurements, Bin Wu of South China University of Technology for XRD measurements, Yanhong Meng for refractive index and extinction coefficient measurements, Xueqing Xu for reflectance measurements and Feng Liu for critical reading of the manuscript. H.W. and Y.C. acknowledge financial support from the National Basic Research Program of China (no. 2009CB623602), the National Nature Science Foundation of China (nos 50990065, 51010003, 60906032 and 61177022), the Program for New Century Excellent Talents in University (NCET-10-0400) and Fundamental Research Funds for the Central Universities (2009ZZ0047).

Author contributions

H.W., Z.H. and C.Z. conceived the idea and designed the experiments. Z.H. fabricated and characterized the devices. C.Z. carried out the optical calculation. S.S. synthesized the interlayer polymer. H.W. and Y.C. coordinated and directed the study. All authors contributed to manuscript preparation, data analysis and interpretation, and discussed the results.

Additional information

Supplementary information is available in the online version of the paper. Reprints and permission information is available online at http://www.nature.com/reprints. Correspondence and requests for materials should be addressed to H.W.

Competing financial interests

The authors declare no competing financial interests.